



Dielectric properties of poly(vinylidene fluoride)-based nanocomposites containing a LaFeO₃ nanoparticle filler

Pornsawan Kum–onsa¹ and Prasit Thongbai^{2,3,*}

¹Materials Science and Nanotechnology Program, Faculty of Science, Khon Kaen University, Khon Kaen 40002, Thailand

²Department of Physics, Faculty of Science, Khon Kaen University, Khon Kaen 40002, Thailand

³Institute of Nanomaterials Research and Innovation for Energy (IN-RIE), NANOTEC-KKU RNN On Nanomaterials Research and Innovation for Energy, Khon Kaen University, Khon Kaen 40002, Thailand

Received: 18 February 2021

Accepted: 13 April 2021

Published online:
29 April 2021

© The Author(s), under exclusive licence to Springer Science+Business Media, LLC, part of Springer Nature 2021

ABSTRACT

Flexible dielectric polymer nanocomposites have been widely investigated in recent years due to their potential application in electronic devices. In this study, a new system of flexible composites is prepared by incorporating the orthorhombic perovskite structure of a LaFeO₃ (LFO) filler into poly(vinylidene fluoride) (PVDF). LFO nanoparticles with an average particle size of ~ 194 nm are synthesized by the combustion method. The effect of the introduced LFO on the morphology, structure, phase composition, and dielectric properties of the composites is investigated. The LFO/PVDF nanocomposites show a large dielectric permittivity, which is approximately 5 times higher than that of pure PVDF. Interestingly, the dielectric loss tangent of the composites is decreased by ~ 0.059 at a volume fraction of LFO ($f_{\text{LFO}} = 0.5$), temperature of ~ 20 °C, and frequency of 1 kHz. The improved dielectric properties of the LFO/PVDF composites can be explained by the presence of strong interfacial polarization and the increase in the polar β -PVDF phase in the nanocomposites. This work provides a comprehensive guideline for improving dielectric polymer nanocomposites with high permittivity and low dielectric loss.

1 Introduction

Materials with excellent dielectric properties have been increasingly studied because of their potential application in many products, such as sensors, embedded capacitors, gate dielectric devices, and energy storage devices [1–6]. There has been an ever-

increasing demand for dielectric materials with high dielectric permittivity (ϵ') and low dielectric loss tangent ($\tan\delta$) over a wide range of frequencies and temperatures. Ceramic materials possess very high ϵ' but are brittle and have low dielectric strength. In contrast, polymers are flexible, easy to process due to

Address correspondence to E-mail: pthongbai@kku.ac.th

their low processing temperatures, and possess high dielectric breakdown fields.

Considerable effort has been made in preparing dielectric composite materials with polymers as the matrix and ceramic particles as the filler to combine the best characteristics of both components. Thus, the combination of ceramics and polymers to form composite materials that demonstrate high ϵ' , flexibility, and a large breakdown strength through a low-temperature process is required for the miniaturization of modern electronic devices.

Generally, poly(vinylidene fluoride–trifluoroethylene) (P(VDF–TrFE)) [7, 8], polyimide (PI) [9, 10], and polyethersulfone (PES) [11] have been used as matrices for composites. In this study, poly(vinylidene fluoride) (PVDF) is selected as the matrix due to its high ϵ' (compared to other copolymers), thermal stability, and easy processing [7, 8]. Ceramics with large values of ϵ' , such as $\text{ACu}_3\text{Ti}_4\text{O}_{12}$ ($A = \text{Ca}, \text{La}_{0.5}\text{Ca}_{0.5}, \text{Na}_{0.5}\text{Y}_{0.5}, \text{Na}_{0.5}\text{Bi}_{0.5}, \text{Na}_{1/3}\text{Ca}_{1/3}\text{Bi}_{1/3}$ [10–17], BaTiO_3 [18], $(\text{Ba},\text{Sr})\text{TiO}_3$ [19], $\text{Ba}(\text{Fe}_{0.5}\text{Nb}_{0.5})\text{O}_3$ [20], and BiFeO_3 [21, 22]), have been used as fillers in polymer-based composites. In addition, orthorhombically distorted perovskite LaFeO_3 (LFO) with the coexistence of antiferromagnetic and ferroelectric–multiferroic properties has been reported in the literature [23–26].

Moreover, LFO can be used as an ethanol sensor and hot electrode for magnetohydrodynamic power generation due to its high electrical conductivity, thermal stability, and high ϵ' (10^3 – 10^5) at room temperature and 1 kHz [23–26]. Therefore, LFO is a new ceramic of the rare-earth orthoferrite family that has been increasingly studied for use as a dielectric material. The aim of this study is to provide a new polymer nanocomposite system with improved dielectric properties.

In this work, LFO nanoparticles are selected as a filler for preparing two-phase PVDF-based composites. LFO nanoparticles are synthesized by combustion using glycine as a fuel. The crystal phase, crystal structure, microstructure, and dielectric properties of the LFO/PVDF nanocomposites are investigated.

2 Experimental section

2.1 Sample preparation

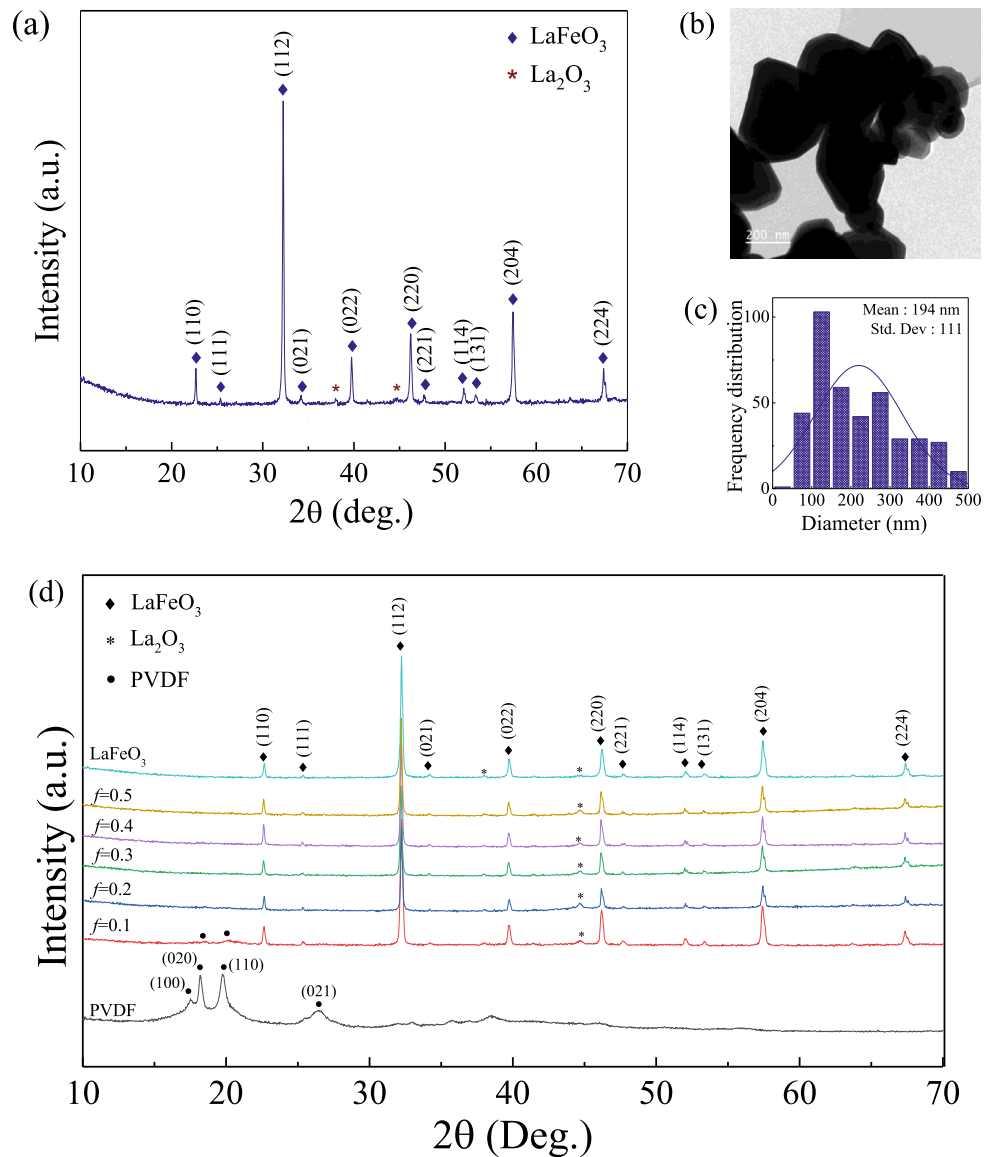
For the preparation of LFO nanoparticles, a combustion method was employed. $\text{LaN}_3\text{O}_9 \cdot 6\text{H}_2\text{O}$ (99.9%, Aldrich), $\text{FeN}_3\text{O}_9 \cdot 9\text{H}_2\text{O}$ (99.9%, Aldrich), $\text{NH}_2\text{CH}_2\text{COOH}$ (99%, ACI Labscan), and CH_3COOH solution (ACI Labscan) were used as raw materials. First, $\text{LaN}_3\text{O}_9 \cdot 6\text{H}_2\text{O}$ and $\text{FeN}_3\text{O}_9 \cdot 9\text{H}_2\text{O}$ were dispersed in a CH_3COOH solution and stirred with a magnetic bar on a hot plate at 25 °C for 1 h. Second, an appropriate amount of $\text{NH}_2\text{CH}_2\text{COOH}$ was added to the homogenous solution with continuous stirring. Third, the solution was heated to 150 °C to form a wet gel. Then, the resultant gel was combusted at 350 °C for 0.5 h. Next, the dried precursor powder was calcined at 1000 °C for 10 h. Finally, LFO nanoparticles were obtained at 25 °C.

For the preparation of the two-phase LFO/PVDF nanocomposites, liquid-phase-assisted dispersion and hot-pressing methods were used. The calcined LFO powder was introduced into PVDF ($M_w \sim 534,000$, Aldrich) in ethanol by ball milling for 3 h. The mixture was transferred into a beaker and dried at 80 °C overnight to remove ethanol. The dried powder was placed in a mold and pressed to form a sample with a diameter of ~ 12 mm and a thickness of 0.7–1 mm. The LFO/PVDF nanocomposites with $f_{\text{LFO}} = 0, 0.1, 0.2, 0.3, 0.4,$ and 0.5 were kept at room temperature.

2.2 Sample characterization

The surface morphology of the LFO nanoparticles was examined by transmission electron microscopy (TEM, FEI Tecnai G2 20). The phase composition and crystal structures of the LFO powder, PVDF polymer, and LFO/PVDF nanocomposites were characterized using X-ray diffraction (XRD; PANalytical, EMPYR-EAN). The fractured surface morphology of each LFO/PVDF nanocomposite was investigated using focused ion beam—field emission scanning electron microscopy (FIB – FESEM, FEI Helios Nanolab G3 CX). To investigate the fractured surface morphology, samples were fractured by liquid N_2 and sputtered with gold. The crystal phase of the LFO/PVDF nanocomposites was analyzed by Fourier transform infrared (FTIR) spectroscopy (Bruker, TENSOR27). Before the dielectric measurements, silver was

Fig. 1 **a** XRD pattern of the LFO powder, **b** TEM image of the LFO nanoparticles, **c** size distribution of the LFO nanoparticles, and **d** XRD patterns of the LFO/PVDF nanocomposites with various volume fractions of LFO nanoparticles



printed on both surfaces of the samples. The dielectric properties of all samples were recorded using an impedance analyzer (KEYSIGHT, E4990A) at an AC oscillation voltage of 0.5 V, a frequency range of $10^2 - 10^6$ Hz, and a temperature range of -60 °C to 150 °C.

3 Results and discussion

To determine the crystal phase of LFO, XRD patterns were recorded. Figure 1a presents the XRD pattern of the LFO nanoparticles. The diffraction peaks of the sample were indexed based on the orthorhombic phase (JCPDS 74 – 2203) [24, 26] with a perovskite

crystal structure (space group *Pbnm*). The diffraction peaks at 2θ corresponded to (110), (111), (112), (021), (022), (220), (221), (114), (131), (204), and (224) planes, confirming the formation of LFO. However, XRD peaks belonging to the impurity phase of La₂O₃ were detected. During the calcination process, La₂O₃ and Fe₂O₃ nanoparticles were formed first, and then these two phases reacted together to form the final product of the LFO phase. However, a small amount of residual La₂O₃ was detected, which may be due to an incomplete reaction. This residual impurity phase could be eliminated by increasing the calcination temperature; however, the obtained particle sizes were largely increased, and a coarse powder was obtained. This coarse powder was unsuitable for use

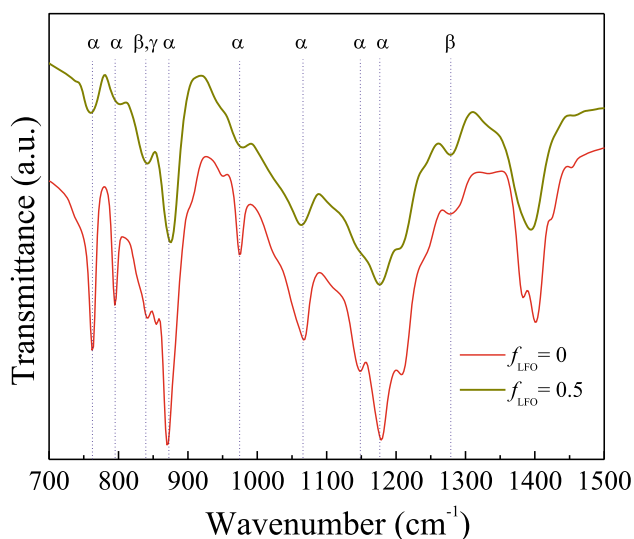


Fig. 2 FTIR spectra of the LFO/PVDF nanocomposites with $f_{\text{LFO}} = 0$ and 0.5

Table 1 Vibrational mode wavenumbers of the LFO/PVDF composites with $f_{\text{LFO}} = 0$ and 0.5

Band (cm^{-1})	Group and vibrational mode	Phase
762	$\delta(\text{CF}_2) + \delta(\text{CCC})$	α
795	$r(\text{CH}_2)$	α
841	$r(\text{CH}_2) - v_s(\text{CF}_2)$	β, γ
870	$v_s(\text{CC}) + \delta(\text{CCC}) + v_s(\text{CF}_2)$	α
974	$t(\text{CH}_2)$	α
1067	$v_s(\text{CC})$	α
1148	$V_{\text{as}}(\text{CC}) - v_s(\text{CF}_2)$	α
1179	$v_s(\text{CF}_2) + t(\text{CH}_2)$	α
1277	$v_s(\text{CF}_2) - v_s(\text{CC}) + \delta(\text{CCC})$	β

v_s symmetric stretching, v_{as} asymmetric stretching, δ bending, t twisting, r rocking, CC CC skeletal vibration, CCC CCC skeletal vibration

as a ceramic filler to improve the dielectric properties of a PVDF polymer matrix. By taking into account the small amount of the La_2O_3 phase and the low ϵ' of the La_2O_3 ceramic compared to that of the LFO ceramic, the effect of the La_2O_3 impurity could be ignored.

The TEM image of the LFO morphology (Fig. 1b) revealed that the LFO nanoparticles had a smooth surface. This result showed that LFO nanoparticles had a non-spherical shape. The particle size distribution of LFO was 194 nm, as shown in Fig. 1c. It was observed that the distribution of particle size was irregular and not a typical normal distribution curve. LFO nanoparticles were prepared by a chemical

combustion method. Generally, the combustion and associated energy in processing were difficult to control, and the temperature rapidly increased in a few seconds [27]. Thus, a broad range of particle sizes was obtained.

Figure 1d shows the XRD patterns of the LFO/PVDF nanocomposites with various volume fractions of LFO nanoparticles (f_{LFO}). The XRD pattern of the PVDF ($f_{\text{LFO}} = 0$) polymer exhibited a semicrystalline structure of the α -phase, corresponding to the (110), (020), (110), and (021) planes. As f_{LFO} increased to 0.2, the diffraction peaks of PVDF almost disappeared. The decrease in the intensity of PVDF indicated that the crystallinity of the PVDF polymer could be influenced by the incorporation of ceramic fillers (LFO). The diffraction peaks of all the LFO/PVDF nanocomposites matched the standard pattern of LFO (JCPDS 74 – 2203), confirming that the LFO/PVDF nanocomposites consisted of LFO with a small amount of the La_2O_3 impurity.

The formation of any PVDF phase has a large effect on the dielectric properties of PVDF–matrix nanocomposites. Because the XRD peaks of a PVDF polymer cannot be detected in the LFO/PVDF nanocomposites, the phase compositions (e.g., α -, β -, and γ -phases) of a PVDF polymer in the nanocomposites cannot be quantified. Therefore, the crystallization of LFO/PVDF nanocomposites was further investigated by FTIR for the identification and quantification of the PVDF polymer phase, as shown in Fig. 2. Transmittance bands at 841 and 1277 cm^{-1} were observed and assigned to the β -phase [7, 28–30]. Additionally, the band at 841 cm^{-1} corresponded to the γ -phase [7, 28–30]. The characteristic bands of the α -phase at 762, 795, 870, 974, 1067, 1148, and 976 cm^{-1} [7, 28–30] were presented in both nanocomposites with $f_{\text{LFO}} = 0$ (pure PVDF) and 0.5, but the intensity of the α -phase peaks decreased with the introduction of the LFO filler. In addition, the FTIR peaks of the LFO/PVDF nanocomposites, as mentioned above, were identified with different vibration groups, as listed in Table 1. The quantification of the β -phase fraction ($F(\beta)$) was performed by considering the relative absorption intensity of the β -phase (841 cm^{-1}) and α -phase (762 cm^{-1}). Details for the calculation were explained in previous studies [17, 31]. It was observed that the $F(\beta)$ values of the nanocomposites with $f_{\text{LFO}} = 0$ and 0.5 were found to be 0.444 and 0.614, respectively. This result showed that the introduction of LFO nanoparticles into the

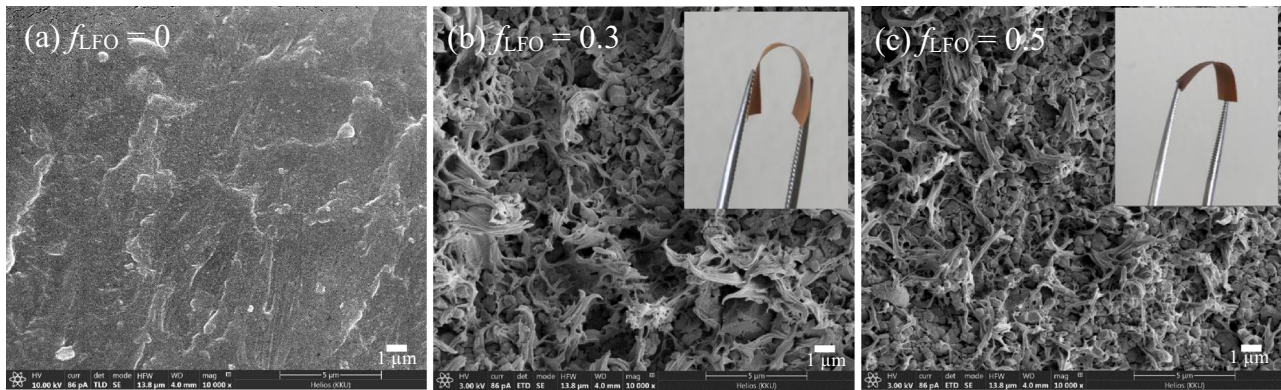


Fig. 3 SEM cross-sections of the LFO/PVDF nanocomposites with $f_{\text{LFO}} = 0, 0.3,$ and 0.5 ; insets of **b** and **c** show flexible nanocomposites with $f_{\text{LFO}} = 0.3$ and 0.5 , respectively

PVDF matrix led to an increased β -phase in the sample. The polar β -phase of PVDF was the most desirable for providing better dielectric properties [32].

Figure 3 shows SEM images of the fractured cross-sections of nanocomposites with $f_{\text{LFO}} = 0, 0.3,$ and 0.5 . As shown in Fig. 3a, a uniformly pure PVDF polymer was observed. When LFO nanoparticles were added to PVDF, the LFO particles dispersed throughout the matrix, as shown in Fig. 3b. Moreover, the nanocomposites tended to slightly agglomerate with a high content of LFO at $f_{\text{LFO}} = 0.5$, and no obvious pores were observed, as seen in Fig. 3c. It was observed that a continuous, nonporous PVDF polymer phase was formed. When the LFO nanoparticles were incorporated into the PVDF polymer matrix, the LFO nanoparticles were observed to randomly fill in the 3D PVDF matrix. This observation indicated the LFO/PVDF nanocomposites had 0–3 connectivity [33]. Thus, the formation of a continuous PVDF polymer matrix was inhibited by the introduction of LFO nanoparticles, thereby promoting the formation of a small number of pores. Generally, the distribution of filler usually plays a remarkable role in the dielectric properties of a composite. Clearly, the homogeneous dispersion of filler in a composite is preferable to provide better dielectric properties than that of a composite containing a large agglomeration of filler particles. It is important to note that when the LFO/PVDF nanocomposite films were fabricated, highly flexible nanocomposites could be obtained, as shown in the insets of Fig. 3b and c.

The frequency dependence of the ϵ' , $\tan\delta$, and AC conductivity (σ_{ac}) values of LFO/PVDF nanocomposites with different f_{LFO} values at room

temperature are shown in Fig. 4. The ϵ' value of the nanocomposites decreased with an increased frequency, especially with a high content of LFO, as revealed in Fig. 4a. The decrease in ϵ' as the frequency increased may be explained on the basis of a decrease in polarization with an increase in frequency. The polarization of a dielectric material includes the contributions of the interfacial, dipolar, ionic/atomic, and electronic polarizations. At a low frequency, all the polarizations can easily respond to the time variation of the AC electric field. However, as the frequency of the AC electric field increased, different polarization contributions were filtered out. Generally, the electrical responses of the ionic/atomic and electronic polarizations could occur at frequencies higher than the GHz region, while the interfacial and dipolar polarizations could respond to the AC electrical field at a relatively lower frequency than those of the other two polarizations [34, 35]. As a result, the net polarizations of the composites that were contributed by the interfacial and dipolar polarizations decreased, which led to a decrease in the ϵ' [36]. The ϵ' of the LFO/PVDF nanocomposite with $f_{\text{LFO}} = 0.5$ linearly decreased with an increasing frequency from 10^2 to 10^6 Hz, indicating that the primary contribution of the interfacial polarization occurred in the nanocomposites. The LFO/PVDF nanocomposites showed ϵ' at 1 kHz of $\sim 25.5, \sim 34.2, \sim 38.6, \sim 42.3,$ and ~ 54.6 with $f_{\text{LFO}} = 0.1, 0.2, 0.3, 0.4,$ and 0.5 , respectively. The increase in ϵ' with an increased LFO loading was a result of a strong interfacial polarization phenomenon, which occurred at the interface between the semiconducting LFO nanoparticles and the insulating PVDF polymer matrix. The charge carriers in the LFO particles were

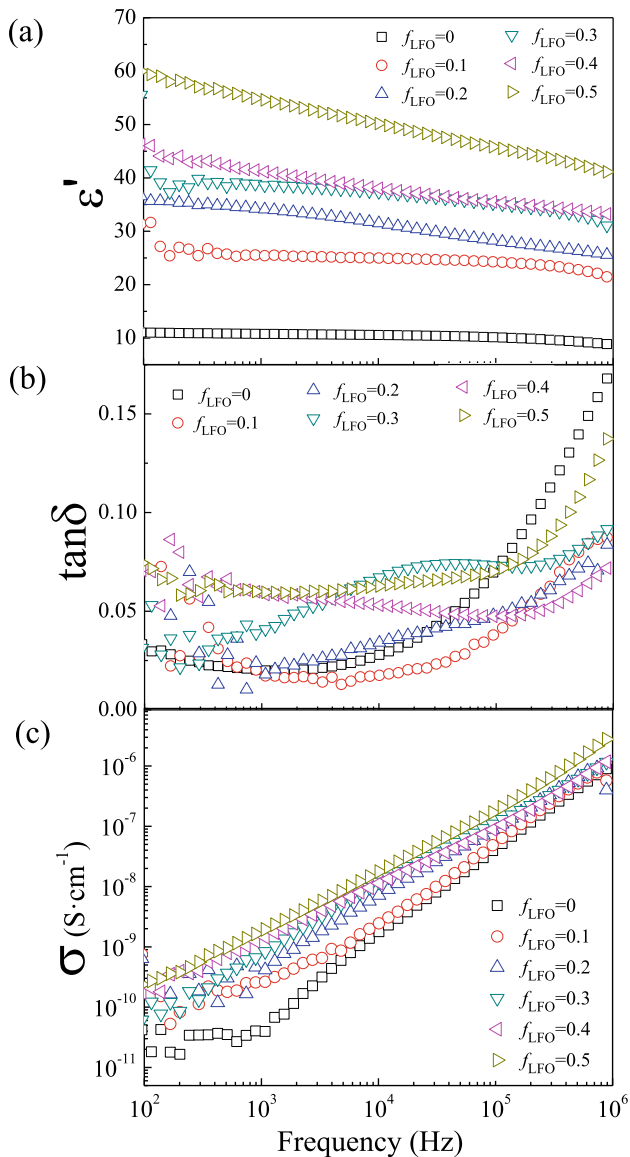


Fig. 4 Frequency dependence of **a** ϵ' , **b**, $\tan\delta$, and **c** σ_{ac} for the LFO/PVDF nanocomposites with different f_{LFO} at room temperature

trapped at the interface of the different phases in the composites, resulting in an increase in ϵ' [37]. The observed enhancement of the ϵ' value of the nanocomposites could be explained from the microstructural point of view that was based on the interfacial polarization [38–40]. The adjacent semiconducting LFO nanoparticles, which were separated by a dielectric layer of PVDF polymer, were considered internal electrodes. This local microstructure in the nanocomposites could create an internal barrier layer capacitor (IBLC). Free charges in the internal electrodes of the semiconducting LFO nanoparticles

could move under an applied electric field and get trapped at the surface of the insulating PVDF polymer. These trapped charges produced an interfacial polarization, leading to an enhancement in ϵ' . The number of IBLC units in the nanocomposites depended on the number of internal electrodes, which increased with an increasing f_{LFO} . Therefore, the increased ϵ' of the nanocomposites due to the increased f_{LFO} could be described in this way. However, it was observed that the increasing trend did not obey the increasing trend of the additive mass ratio. These deviations may be associated with the induced interfacial polarization, since more nanoparticles generally tended to aggregate as the f_{LFO} increased. Consequently, the interfacial polarization slowly increased even when the f_{LFO} continuously increased. According to the FTIR results, the polar β -phase of the PVDF polymer was induced to increase by incorporating LFO nanoparticles. Thus, the significant increase in the ϵ' of the LFO/PVDF nanocomposites compared to that of the PVDF polymer was also contributed by the increased β -PVDF phase in the composites [17, 31].

Moreover, it was seen (Fig. 4b) that the $\tan\delta$ of the nanocomposites slightly increased in the high frequency range over 10^5 Hz; this result was attributed to the α_a relaxation, which is associated with the glass transition of a pure PVDF polymer [41, 42]. Interestingly, the $\tan\delta$ values of the LFO/PVDF nanocomposites for all compositions were lower than 0.06 at 1 kHz. Notably, the LFO/PVDF nanocomposite with $f_{LFO} = 0.5$ exhibited a significantly increased ϵ' 54.6 and low $\tan\delta \sim 0.059$ at 1 kHz. As summarized in Table 2, comparing the dielectric properties of the LFO/PVDF nanocomposites at 1 kHz with different composite systems showed that the LFO/PVDF nanocomposite system was one of the most interesting two-phase ceramic/polymer composites. As seen in Fig. 4c, the AC conductivity (σ_{ac}) increased linearly with an increasing frequency. The values were lower than 10^{-8} S·cm $^{-1}$ at 1 kHz even when the loading of f_{LFO} filler was up to 0.5, indicating that no conductive network or pathway formed in the nanocomposites.

To identify the influence of temperature on the dielectric behavior of the LFO/PVDF nanocomposites, ϵ' and $\tan\delta$ were measured from -60 °C to 150 °C, as shown in Fig. 5. The ϵ' and $\tan\delta$ of the LFO/PVDF nanocomposites exhibited a temperature dependence, especially at high temperature. This

Table 2 Comparison of ϵ' and $\tan\delta$ (at 1 kHz and $\sim 25^\circ\text{C}$) of the LFO/PVDF nanocomposites with various ceramic/polymer compositions

Polymer matrix composites	Volume fraction of the filler	1 kHz		References
		ϵ'	$\tan\delta$	
CaCu ₃ Ti ₄ O ₁₂ /PVDF	52 vol%	~ 40	~ 0.1	[12]
CaCu ₃ Ti ₄ O ₁₂ /PVDF	50 vol%	~ 65	~ 0.1	[13]
CaCu ₃ Ti ₄ O ₁₂ /PVDF	50 wt%	53	0.07	[14]
La _{0.5} Ca _{0.5} Cu ₃ Ti ₄ O ₁₂ /PVDF	50 wt%	69	0.09	
Na _{0.5} Bi _{0.5} Cu ₃ Ti ₄ O ₁₂ /PVDF	50 vol%	~ 100	~ 0.11	[15]
Na _{1/3} Ca _{1/3} Bi _{1/3} Cu ₃ Ti ₄ O ₁₂ /PVDF	50 vol%	156	0.075	[16]
Na _{0.5} Y _{0.5} Cu ₃ Ti ₄ O ₁₂ /PVDF	50 vol%	84	0.11	[17]
BaTiO ₃ /PVDF	40 vol%	61.9	0.22	[18]
BaTiO ₃ /PVDF film		623.3	0.89	
(Ba,Sr)TiO ₃ /PVDF film	40 vol%	40	0.19	[19]
Ba(Fe _{0.5} Nb _{0.5})O ₃ /PVDF	50 vol%	~ 65	~ 0.11	[20]
BiFeO ₃ /PVDF film	50 vol%	~ 105	~ 0.5	[21]
BiFeO ₃ /PMMA film	30 vol%	32	0.25	[22]
LFO/PVDF	50 vol%	54.6	0.059	This work

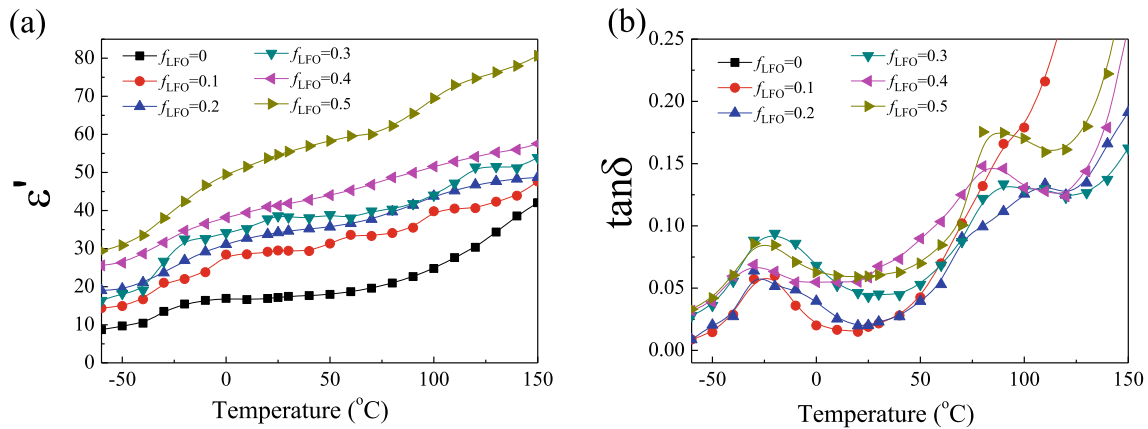


Fig. 5 Temperature dependence of **a** ϵ' and **b** $\tan\delta$ for the LFO/PVDF nanocomposites with different f_{LFO} at 1 kHz

phenomenon was attributed to the chain mobility and thermal expansion of the PVDF matrix. Thus, ϵ' and $\tan\delta$ remarkably changed in the high temperature range. The $\tan\delta$ of nanocomposites exhibited 2 relaxation peaks at approximately -35°C and above 40°C , which are known as the β -relaxation and α -relaxation of a PVDF polymer, respectively [43].

4 Conclusion

Two-phase PVDF-based polymer composites with LFO nanoparticles were prepared using liquid-phase-assisted dispersion and hot-pressing methods. The LFO nanoparticles were synthesized by a combustion method using glycine as fuel. Compared to pure PVDF, the introduction of LFO into the PVDF

matrix increased ϵ' . Moreover, the dielectric permittivity of the composite films exhibited a large dependence on LFO, which induced notable interfacial polarization. Furthermore, the addition of LFO nanoparticles into the PVDF polymer also promoted the formation of the β -PVDF phase, increasing the ϵ' values of the composites. Thus, the addition of LFO nanoparticles resulted in improved dielectric properties, which was demonstrated to be an effective way to enhance the high ϵ' of the LFO/PVDF nanocomposites.

Acknowledgements

This work was financially supported by the Basic Research Fund of Khon Kaen University and the

Institute of Nanomaterials Research and Innovation for Energy (IN–RIE), Khon Kaen University. P. Kumonsa received funding from the Science Achievement Scholarship of Thailand.

References

1. M. Arbatti, X. Shan, Z.Y. Cheng, *Adv. Mater.* **19**, 1369–1372 (2007)
2. L. Ramajo, M.a.M. Reboredo, M.S. Castro, *International Journal of Applied Ceramic Technology* no-no (2009)
3. L. Shaohui, Z. Jiwei, W. Jinwen, X. Shuangxi, Z. Wenqin, *ACS Appl. Mater. Interfaces.* **6**, 1533–1540 (2014)
4. S. Liu, S. Xue, B. Shen, J. Zhai, *Appl. Phys. Lett.* **107**, 032907 (2015)
5. L. Su, Y. Wang, Y. Sha, M. Hao, *J. Alloy. Compd.* **656**, 585–589 (2016)
6. S. Liu, B. Shen, H. Hao, J. Zhai, *J. Mater. Chem. C* **7**, 15118–15135 (2019)
7. P. Martins, A.C. Lopes, S. Lanceros-Mendez, *Prog. Polym. Sci.* **39**, 683–706 (2014)
8. V.K. Prateek, R.K. Thakur, Gupta. *Chem Rev* **116**, 4260–4317 (2016)
9. Y.-H. Wu, J.-W. Zha, Z.-Q. Yao, F. Sun, R.K.Y. Li, Z.-M. Dang, *RSC Adv.* **5**, 44749–44755 (2015)
10. Y. Yang, B.-P. Zhu, Z.-H. Lu, Z.-Y. Wang, C.-L. Fei, D. Yin, R. Xiong, J. Shi, Q.-G. Chi, Q.-Q. Lei, *Appl. Phys. Lett.* **102**, 042904 (2013)
11. F. Wang, D. Zhou, Y. Hu, *Phys. Status Solidi* **206**, 2632–2636 (2009)
12. W. Yang, S. Yu, R. Sun, R. Du, *Acta Mater.* **59**, 5593–5602 (2011)
13. P. Thomas, K.T. Varughese, K. Dwarakanath, K.B.R. Varma, *Compos. Sci. Technol.* **70**, 539–545 (2010)
14. A. Srivastava, K.K. Jana, P. Maiti, D. Kumar, O. Parkash, *Mater. Res. Bull.* **70**, 735–742 (2015)
15. Y.-L. Su, C. Sun, W.-Q. Zhang, H. Huang, *J. Mater. Sci.* **48**, 8147–8152 (2013)
16. P. Kum–onsa, P. Thongbai, *Materials Chemistry and Physics* **256**, (2020)
17. P. Kum-onsa, P. Thongbai, *Mater. Today Comm.* **25**, 101654 (2020)
18. K. Silakaew, W. Saijingwong, K. Meeporn, S. Maensiri, P. Thongbai, *Microelectron. Eng.* **146**, 1–5 (2015)
19. G. Hu, F. Gao, J. Kong, S. Yang, Q. Zhang, Z. Liu, Y. Zhang, H. Sun, *J. Alloy. Compd.* **619**, 686–692 (2015)
20. Z. Wang, M. Fang, H. Li, Y. Wen, C. Wang, Y. Pu, *Compos. Sci. Technol.* **117**, 410–416 (2015)
21. S. Dash, R.N.P. Choudhary, M.N. Goswami, *J. Alloy. Compd.* **715**, 29–36 (2017)
22. M.K. Mishra, S. Moharana, B. Behera, R.N. Mahaling, *Front. Mater. Sci.* **11**, 82–91 (2017)
23. M. Idrees, M. Nadeem, M. Atif, M. Siddique, M. Mehmood, M.M. Hassan, *Acta Mater.* **59**, 1338–1345 (2011)
24. V.M. Gaikwad, S.A. Acharya, *RSC Adv.* **5**, 14366–14373 (2015)
25. E. Cao, Y. Qin, T. Cui, L. Sun, W. Hao, Y. Zhang, *Ceram. Int.* **43**, 7922–7928 (2017)
26. A. Mitra, A.S. Mahapatra, A. Mallick, A. Shaw, N. Bhakta, P.K. Chakrabarti, *Ceram. Int.* **44**, 4442–4449 (2018)
27. M.N. Rahaman, Ebook Library., *Ceramic processing and sintering*, Materials engineering 23, M. Dekker, New York, 2003, pp. 1 online resource (xiii, 875 p.).
28. Y. Bormashenko, R. Pogreb, O. Stanevsky, E. Bormashenko, *Polymer Testing - POLYM TEST* **23**, 791–796 (2004)
29. C. Ribeiro, C.M. Costa, D.M. Correia, J. Nunes-Pereira, J. Oliveira, P. Martins, R. Gonçalves, V.F. Cardoso, S. Lanceros-Méndez, *Nat Protoc* **13**, 681–704 (2018)
30. H.-C. Yang, Q.-Y. Wu, H.-Q. Liang, L.-S. Wan, Z.-K. Xu, *J. Polym. Sci., Part B: Polym. Phys.* **51**, 1438–1447 (2013)
31. P. Kum-onsa, N. Chanlek, B. Putasaeng, P. Thongbai, *Ceram. Int.* **46**, 17272–17279 (2020)
32. S. Liu, S. Xue, W. Zhang, J. Zhai, G. Chen, *J. Mater. Chem. A* **2**, 18040–18046 (2014)
33. J.F. Tressler, S. Alkoy, A. Dogan, R.E. Newnham, *Compos. A Appl. Sci. Manuf.* **30**, 477–482 (1999)
34. A.J. Moulson, J.M. Herbert, *Electroceramics: Materials, Properties, Applications*, 2nd edn. (Wiley, Chichester, 2003).
35. K.-C. Kao, *Dielectric phenomena in solids : with emphasis on physical concepts of electronic processes*, Academic Press, Amsterdam ; Boston, 2004.
36. P. Kumar, P. Mishra, S. Sonia, *J. Inorg. Organomet. Polym Mater.* **23**, 539–545 (2012)
37. S. George, M.T. Sebastian, *Compos. Sci. Technol.* **69**, 1298–1302 (2009)
38. P. Liu, Z. Yao, J. Zhou, Z. Yang, L.B. Kong, *J Mater. Chem. C* **4**, 9738–9749 (2016)
39. P. Liu, V.M.H. Ng, Z. Yao, J. Zhou, Y. Lei, Z. Yang, H. Lv, L.B. Kong, *ACS Appl. Mater. Interfaces.* **9**, 16404–16416 (2017)
40. P. Liu, Z. Yao, J. Zhou, *High Perform. Polym.* **28**, 1033–1042 (2015)
41. K. Yu, Y. Niu, Y. Zhou, Y. Bai, H. Wang, C. Randall, *J. Am. Ceram. Soc.* **96**, 2519–2524 (2013)
42. Y. Song, Y. Shen, P. Hu, Y. Lin, M. Li, C.W. Nan, *Applied Physics Letters* **101**, (2012)

43. A.C. Lopes, C.M. Costa, R.S.I. Serra, I.C. Neves, J.L.G. Ribelles, S. Lanceros-Méndez, *Solid State Ionics* **235**, 42–50 (2013)

Publisher's Note Springer Nature remains neutral with regard to jurisdictional claims in published maps and institutional affiliations.